IMAGE TRANSFORMATIONS AND PRINTING OF PLASTER LAYERS IN SPIRAL GROWTH MANUFACTURING

C. Hauser[+], D.M. Lewis[†], M. Dunschen*, M. Egan[+] , C. Sutcliffe[+].
[+]MSERC, Department of Engineering, University of Liverpool, UK
[†]Department of Colour and Polymer Chemistry, University of Leeds, UK
*FreeSteel, Liverpool, UK (www.freesteel.co.uk)

Abstract

Spiral growth manufacturing (SGM) is a high speed rapid manufacturing technique in which objects are built up, layer by layer, by simultaneously depositing, levelling and selectively consolidating thin powder layers onto a rotating build platform. The size and position of the jetted droplets are mapped by the position and greyscale level of pixels within an 8 bit greyscale bitmap image. This paper reports on the development of software in which mathematical algorithms apply geometric transformations to images in preparation for printing onto a rotating substrate. In support of this work, dimensional accuracy measurements of printed images and methods to correct radial print density variations are reported. The accuracy of printed images were found to be within ±0.2mm of their predicted size. The experimental work is briefly extended to the direct printing of plaster layers, formed by mixing two reactive ink solutions.

Introduction

Three Dimensional Printing (3DP) was developed at the Massachusetts Institute of Technology in the late 1980's [1-3]. It is a layered manufacturing process that builds parts by the repetitive deposition of thin horizontal powder layers, regions of which are selectively solidified by inkjet printing a binder from a scanning print head. The application of the binder also bonds consecutive layers together. The build process is completed with the removal of unbound supporting powder followed by part infiltration (e.g. resin or wax) to increase durability [4]. As with most layer manufacturing technologies, the build methodology is fundamentally a start-stop process since the deposition and processing of each layer occurs sequentially. Hence, the build cycle can be slow, particularly if the build area is large or hardware needs positioning i.e. print heads and powder feeders. Therefore, this technology has largely remained a design prototyping tool or for the manufacture of short run components and tooling. Nevertheless, commercial 3DP technologies are extremely fast in comparison with many other layer manufacturing processes and are capable of building parts at up to 2-6 layers per minute [5].

In an attempt to decrease build time, improve system efficiency and broaden the range of viable materials, The University of Liverpool (UoLiv), in collaboration with The University of Leeds (UoLds) and Inovink Ltd, Sheffield, are developing a 3DP process which prints layers of reaction hardenable material directly onto a rotating substrate. During the rotation the substrate continuously falls away from arrays of stationary print heads allowing layers to form one on top of the other. Hence, the substrate rotates in a spiralling motion with a pitch equating to the more familiar layer thickness. The print heads used are OmniDot 760 industrial print heads (XaarJet Ltd, Cambridge, UK). They are wide format (53.8mm swathe) and can print a full swathe in a single pass; this eliminates the need to raster them for area coverage. The inks are two-part solutions, jetted from different print heads which combine on the substrate and react to form calcium sulphate (Plaster-of-Paris). These inks are currently subject to patent review and so only their use will be discussed here. By printing material directly it removes the need to deposit

powder layers. This gives the ability to create a layer approaching the maximum print speed of the print head (~500mm/s linear print speed or ~30 layers/minute using the SGM configuration discussed in *Equipment and Experimental Methods*). For comparison, deposition of plaster powder layers onto a rotating substrate proved difficult above 12rpm and was limited by poor powder flow properties. The results of this work will be the focus of a future paper.

To successfully print an image using SGM, images must first undergo a series of geometric transformations to correct for the annular distortion and parallax shift (a consequence of the dual nozzle row design of the Xaar print heads) caused by printing onto a rotating substrate. This paper reports on the development of computational algorithms to perform these transformations. Python programming language was used in the development of the algorithms [6,7]. The dimensional accuracy of transformed images was tested by experimentation in which images of different size, shape, complexity and radial placement were printed onto paper using ink formulations similar in composition to the reactive inks but with dyes added for print clarity (although non reactive in this instance). A corrective binary FM screening algorithm was also developed and tested which introduced white noise to monochrome images to homogenise radial print density variations. These experiments were then extended to the printing of the reactive inks. At the time of writing this paper, the reactive inks were not compatible with the OmniDot 760 print head. As a consequence, development work was conducted on a HP DeskJet 5550 printer.

Image Transformations

A digital image in which pixels are defined in Cartesian space will, when printed onto a rotating substrate, undergo a polar distortion. The effect of this distortion, by its simplest interpretation, converts horizontal lines to circular arcs and vertical lines to rays radiating out from the origin of the rotation (see Figure 1a). In the process, a typical pixel, P_a, in the x,y plane will be distorted into a curvilinear pixel, P_d, represented in the figure in the u,v plane. Therefore, the first computational step is to remap pixels from Cartesian to Polar coordinate positions. The coordinate system used in the calculations starts at, $x = 0, y = 0$, in the upper left corner of an image and the coordinates refer to positions between pixels. The position of pixels, P_t, in the transformed image are described in a similar manner but are represented by the Cartesian coordinates, u,v. The position of pixels in the printed transformed image are again described in x,y. The baseline print density in this work is 360 dpi. This is the radial print density, dpi_x, and is calculated from the nozzle density across the print head (14.2 nozzles/mm). Finally, all measurements in this work are in pixels unless otherwise stated.

To start, an 8 bit greyscale or monochrome image is numerically positioned so that its central horizontal axis aligns with an arbitrary radial line and the first column of pixels in the image are at a distance, $cx + px$. Where, cx, is the radial distance of the first nozzle in the print head and ,px, is the position of the image within the print swathe. In the following calculations, $px = 0$. The size of the image after the polar transformation is then calculated. In the image size calculation, the width, su, of the transformed image is a measure of the distance between the pixel closest to and furthest away from the centre of rotation and is given by (see Figure 1b):

$$su = r_{p_{a=n}} - cx \qquad \text{where,} \qquad r_{p_{a=n}} = \sqrt{(cx + sx - 1)^2 + ((sy/2) - 1)^2} \qquad (1)$$

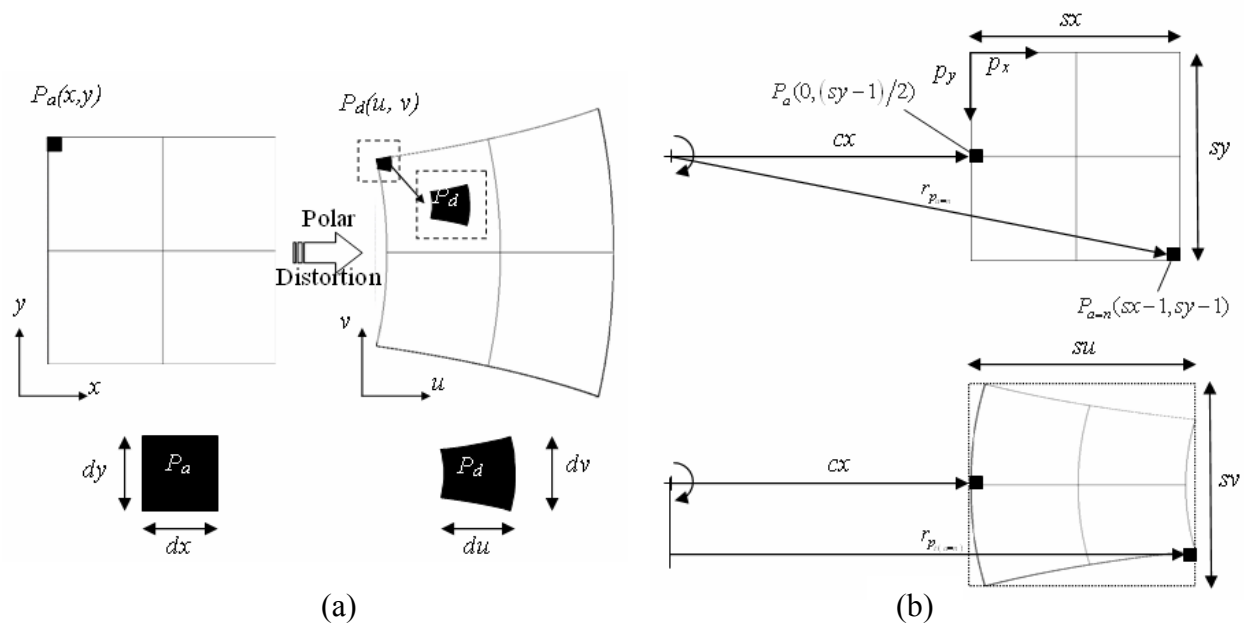

Figure 1: (a) The affect of a polar distortion on a pixelated image and (b) calculating the width, s*u*, of a transformed image.

The value, -1, is included in equations 1 because distances are taken from between pixels i.e. the coordinates of the first pixel in the image are (0,0). The height, s*v*, of the transformed image is dependant on the radial position, *cx*, of the image to be printed and is the product of the length of the arc, v_p, subtended by the original image height, s*y*, during the rotation (see Figure 2a) and the ratio of the circumferential print density, dpi_y, at, *cx*, and the radial print density, dpi_x:

$$sv = \frac{dpi_y}{dpi_x} \cdot v_p \tag{2}$$

where,

$$v_p = \alpha \cdot cx \qquad \text{and} \qquad \alpha = 2\left(\sin^{-1}\frac{sy}{2cx}\right) \tag{3}$$

In the above equations, α, is measured in radians, dpi_x, has a fixed value of 360 dots per inch (see Section 2.2) and, dpi_y, is interpolated from values measured experimentally (see Section 4). If $0 \le su \le S_{\max}$, where, S_{max}, is the width of the available print swathe, then an 8 bit greyscale transformation image of size, s*u*, s*v*, is created and all cells are initialised with a white pixel. Each pixel, P_a, from the original image is then mapped into a cell in the transformation image. The mapping is governed by a polar transformation algorithm and uses the radial distance, r_{p_a}, extending from the centre of rotation to each pixel, P_a, and the subtended angle, θ_a, to calculate the position coordinates, p_{u_t}, p_{v_t}, of each mapped pixel, $P_{t(a)}$ (see Figure 2b).

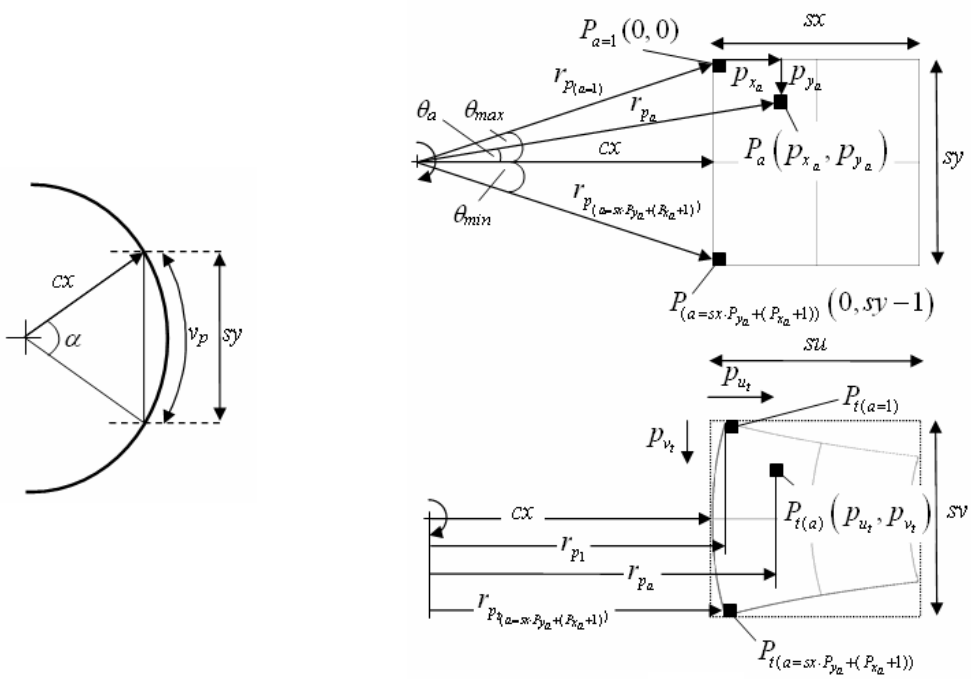

(a) (b)

Figure 2: (a) Calculating the height, s*v*, of a transformed image and (b) Mapping of pixel positions in polar transformation calculations.

The mapping of pixels from one image to another has been accomplished in two different ways; a forward polar transformation and a reverse polar transformation. The reason for the two approaches, including the differences in both methods, will become clear in the following paragraphs. In the forward polar transformation operation, the calculation starts at pixel, $P_{(a=1)}(0,0)$, in the original image and marches through each pixel in number order (from left to right and top to bottom). At every step the radius, r_{p_a}, and the subtended angle, θ_a, from the centre of rotation to each pixel is calculated using;

$$r_{p_a} = \sqrt{\left(\left(cx + p_{x_a}\right)^2 + \left(sy/2 - p_{y_a}\right)^2\right)}, \qquad \theta_a = \tan^{-1}\frac{sy/2 - p_{y_a}}{cx + p_{x_a}} \tag{4}$$

The coordinate, p_{u_t} of each pixel in the transformed image can then be calculated using;

$$p_{u_t} = r_{p_a} - cx \tag{5}$$

The coordinate, p_{v_t}, is a function of the angle, θ_a, and takes the form, $p_{v_t}(\theta_a) = m\theta_a + c$, giving a linear change of, p_{v_t}, from $p_{v_t}(\theta_{\max}) = 0$ to $p_{v_t}(\theta_{\min}) = sv$, where;

$$p_{v_t}\left(\theta_a\right) = \left[\left(\frac{sv}{\theta_{\max} - \theta_{\min}}\right)\cdot\theta_a + \left(\frac{-sv\cdot\theta_{\min}}{\theta_{\max} - \theta_{\min}}\right)\right] \tag{6}$$

Figure 3a shows a typical example, a square (400 x 400 pixels) transformed at different values of, *cx*, using the above methodology. In the figure, the transformed images created at, $dpi_y > dpi_x$, were found to contain unmapped white pixels throughout the transformed image arranged into orderly lines following asymptotic curves. The curves exist when, $sv > sy$, and therefore not all cells in the transformed image are mapped by a pixel in the original image. One approach to overcome this problem is to reduce, dpi_y, by reducing the rate at which ink droplets leave the print head nozzles. This is done by increasing the division of the rotary encoder clock frequency (encoder divide) in the OEM software. However, this method limits the choice and range of print density. This would be particularly restrictive since the density of the printed calcium sulphate is likely to be sensitive to printed density. Furthermore, the clock frequency can only be divided by integer values and so the method is not very accurate. Hence, the sizing of images, in accordance with equation 2, would require constant recalculation. Instead, the preferred method is to run the forward transformation algorithm calculations in reverse order. Using this approach, for each pixel in the transformed image a position in the coordinate system of the original image is found and the pixel located at, or nearest to, the calculated position is mapped into the transformed image. Therefore, the asymptotic curves formed from unmapped pixels disappear (see Figure 3b).

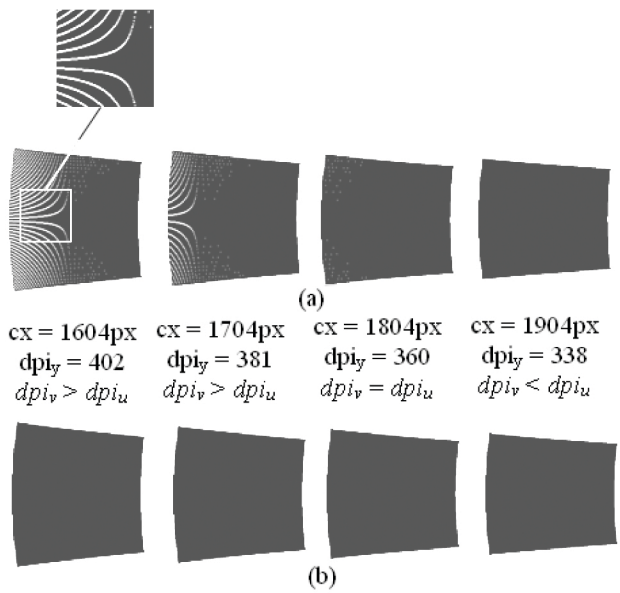

Figure 3: A square image polar transformed using (a) the forward transformation algorithm and (b) the reverse transformation algorithm.

The next step is a linear transformation of the polar transformed image. In the linear transformation, columns of pixels are remapped in the, $\pm v$, direction. This step is necessary because the print head consists of two parallel rows of 382 active nozzles that are positioned in an alternating manner so that a nozzle in one row is either to the left or the right of a nozzle in the other row (see Figure 4a). This arrangement, together with OEM software which offsets the start of firing of one row of nozzles, gives an effective print swathe containing 764 nozzles over a distance of 53.8mm (360dpi or 14.2pixels/mm - baseline). The nozzle row offset, nzr_{off}, is a measure, in pixels in this work, of the firing delay (pitch) between the two nozzle rows and is given by;

$$nzr_{off} = \frac{dpi_y}{25.4} \times \left(d_{nzr}\right) \tag{7}$$

where, d_{nzr}, is the distance in, *mm*, between the two nozzle rows and has a value of 4.233mm. When printing onto a rotating substrate, the print density, dpi_y, at each nozzle changes because the tangential velocity of the substrate at each nozzle is different. Hence, a constant offset, nzr_{off}, across the print head would cause a parallax shift in the printed image (see Figure 4b). The parallax angle, δ_t, when printing a square of size, *su, sv*, (see Equations 1,2) positioned in the print swathe at, *px*, is given by;

$$\delta_t = \tan^{-1}\left(\frac{d_{nzr}}{2(cx + px + su)}\right) \tag{8}$$

Since the OEM software does not support a variable offset across the print head, each column of pixels, Pu_c, in the transformed image must be remapped using vertical displacements in, $\pm v$, direction to achieve the required delay. For alignment purposes, the remapping algorithm is geared to implement a delay in one row of nozzles and an advance in the other so that the printed image axis, *sx*, is parallel to the centre line of the print head. Therefore, the amplitude of

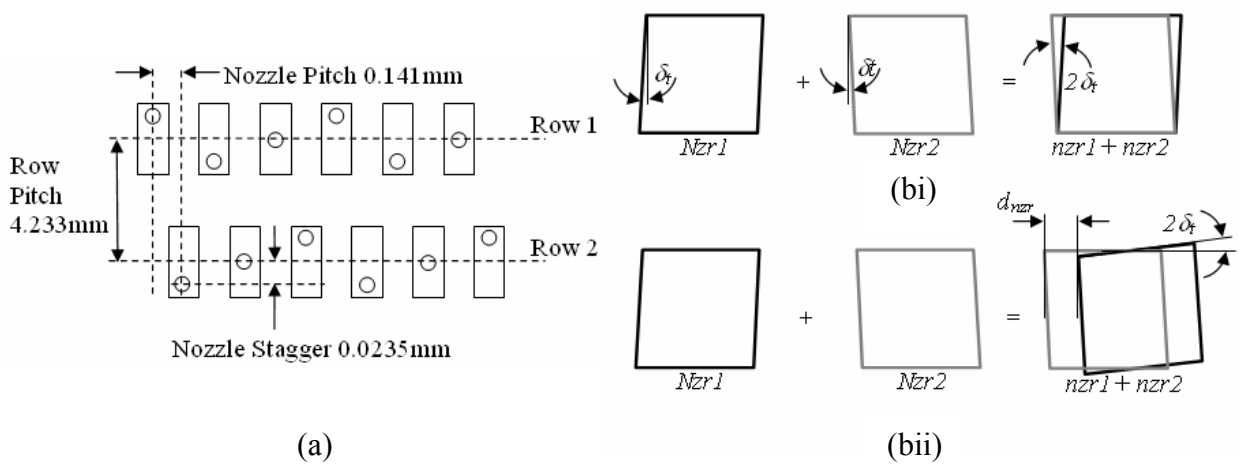

Figure 4: (a) OmniDot 760 GS8 Print head nozzle plate schematic and (b) Effects of a constant nozzle row offset, nzr_{off}, when printing a square bitmap image onto a rotating substrate using (bi) nzr_{off} = 60* @ dpi_y= 360 (bii) $nzr_{off} = 0$.
* Typical offset settings for linear printing.

the displacement is a function of the radial position of the nozzle and the direction of the displacement is dependant on the row in which the corresponding nozzle is located. The amplitude of the displacement, *v*, changes linearly from, $Pu_{c=0} = coff_1$, to, $Pu_{c=763} = coff_2$, where (see Figure 5);

$$coff_1 = \frac{nzr_{off}}{2}, \qquad coff_2 = coff_1 - \left(su \tan \delta_t\right) \tag{9}$$

The default direction of the displacement is set so that all columns of pixels printed by the nozzles in, *nzr1*, move in the, -*v*, i.e. $Pu_{c=0}$, $Pu_{c=2}$, $Pu_{c=4}$...$Pu_{c=762}$, and all columns of pixels printed by the nozzles in, *nzr2*, move in the, +*v*, i.e. $Pu_{c=1}$, $Pu_{c=3}$, $Pu_{c=5}$…$Pu_{c=763}$. The directions can be reversed if the direction of rotation of the substrate and/or print head setup is changed. The nozzles are also staggered, in a repeating pattern of three, across each nozzle row (see Figure 4a). However, the nozzle stagger is significantly less than the nozzle pitch; the latter being used to determine the baseline print density, dpi_x. When printing at, $dpi_y = dpi_x = 360$, the required offset to compensate for nozzle stagger would equate to $1/6$ pixel (0.0235mm /0.141mm); this would be impossible to achieve since only whole pixels can be moved in the transformation software. Full compensation would first be achievable when printing at, dpi_y=2160 (360x6). Since, the effect of nozzle stagger on printed image accuracy is extremely small across relatively large changes in, dpi_y, steps required to compensate for it are not considered in this work.

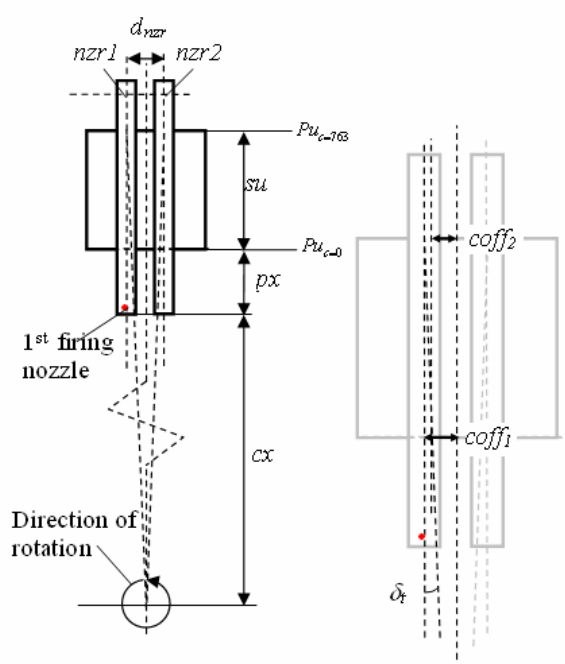

Figure 5: Calculating maximum and minimum nozzle row offset values, $coff_1$, and $coff_2$.

Image Screening

Experimental results (see Figures 6/9) illustrated that the print density, dpi_y, at each nozzle reduced with increasing radius according to the tangent function;

$$\tan\theta = \frac{y}{x} \tag{10}$$

Since the length, y, is an arbitrary constant, $x=cx+px$, and using a suitable scaling factor, X, chosen by curve fitting experimental and calculated data, the print density, dpi_y ,across the available print swathe can be evaluated using;

$$dpi_y = X \cdot cx^{-1} \tag{11}$$

Visually, this effect caused a monochrome image to be printed with shades of grey varying from dark shades at, *cx,* to lighter shades at, (*cx* + *px* + *su)*. To offset radial changes in print density two algorithms were developed. The first algorithm adjusted the grey level intensity of pixels across the image to offset the measured changed in intensity. The Xaar OmniDot 760 print head can produce 5 different drop sizes which directly relate to a small number of discrete pixel intensities distributed across all levels of grey. However, for pixel intensities which fall between these values the associated print head software applied a print pattern to give a perceived impression of grey. The second algorithm made use of digital halftoning techniques to apply FM screening and remove pixels (switch to white) from an image. To start, each column of pixels in an image was grouped into cells. The number of pixels in each cell to be switched was then calculated according to equation 11. The calculated number of pixels were then systematically removed using an equal spacing. This created an image with strong patterning (see Figure 6(i)). To removed patterning, the next step was to randomise the final position of each switched pixel by displacing it within a given tolerance in ±*x* and ±*y*. Figure 6(ii), shows pixel placement with a tolerance of ±(*x* = 15) and Figure 6(iii) shows pixel placement with a tolerance of ±(*x* = 15) and ±(y = 10).

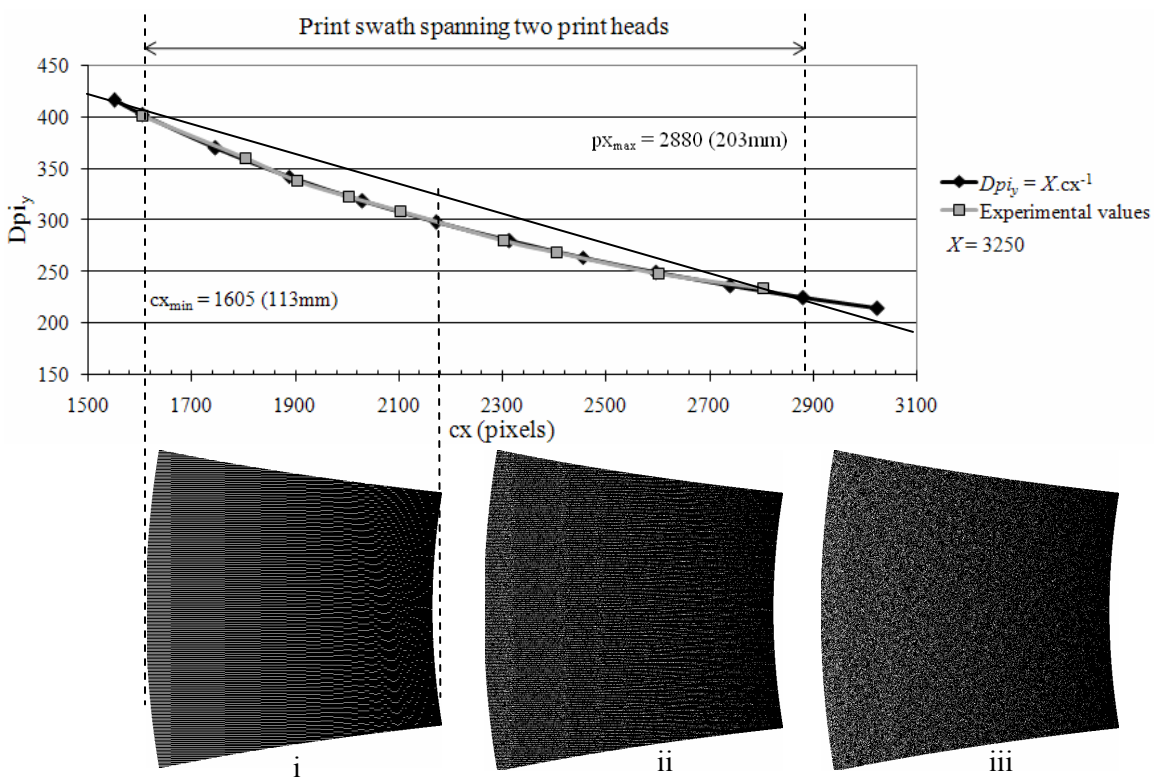

Figure 6: Graph showing experimental and calculated values of changes in print density, dpi_y, with radial position, *cx*. Included are images of a 600x600 pixel square polar transformed then FM screened (i) systematically, (ii) with noise of amplitude ±(*x* = 15pixels) and (iii) with noise of amplitude ±(*x* = 15pixels) and ±(y = 10pixels).

Equipment and Experimental Methods

An SGM machine, designed and built at the UoLiv, was used for all experimental work described in this paper (see Figure 7). The machine consisted of a 500mm x 100mm high rotating build drum, in which, arrays of stationary print heads were positioned to facilitate image printing on the floor or the drum. Figure 7 shows two SGM configurations. Figure 7a shows one array of three print heads in combination with a powder feeder and wiper blade. Figure 7b shows two arrays of three print heads. The latter configuration has been used in this work although both two have been shown to highlight system flexibility and to show a typical configuration for powder deposition. A detailed description of the print heads are given in *image transformations* section of this paper. Two of the three print heads (see Figure 7b) in each array are positioned at different radii, and both centralised on two arbitrary radial lines. This gives an effective wide format print swathe of approx 1275 pixels (90mm) with an overlap region, *ox*, of 253 pixels and a starting radius, *cx*, of 1605 pixels (113mm). The third print head is positioned at the same radii as print head one. This gives the functionality to overprint using the reactive inks. Although not discussed in detail here, the transformation and screening software described earlier is part of a software suite that also includes motion control software and software to position and prepare images for printing across multiple print heads.

During each rotation the drum continuously falls away from the print heads. The drop is driven by a ball screw. The rotational speed of the ball screw is synchronised with the rotation of the drum to give a continuous spiralled layer with a constant pitch. For evaluation purposes, the term 'layers' is still used in this work; where one layer is defined by the completion of one complete revolution of the build drum. Hence, the pitch is controllable and its magnitude gives a fixed point of reference between the top of the build and the print head nozzles. A rotary and linear encoder attached to the drum and ball screw respectively monitors positional changes. The rotary encoder clock pulse is also used to synchronise events in the print heads.

Monochrome bitmap images, included screened images, of squares, rectangles and circle that varied in size were transformed and printed at different values of, *px*, to test for printed size accuracy and reproducibility. The rotational speed ranged from 1 to 35 rpm. All images were printed onto strips of paper that were taped to the floor of the build drum. The ink used in the experiments was an aqueous based ink with blue dye added for print clarity. This ink was a precursor to the reactive inks. The size and diagonal deviation (squareness) of printed images were measured using a microscope with a Vernier scale attached to the stage. The results were then compared to the predicted image size. The predicted size of an image is calculated using the baseline print density of 360 dpi (see *image transformations* section). Greyscale shading of printed images was approximated by digitising the printed image (using an Epson 2480 photo scanner) then measuring the grey level of pixels at equal intervals across the image using Adobe Photoshop™ software (using the eyedropper tool set to a 5x5 average pixel sample).

Multiple layer passes using the reactive inks was carried out using a HP DeskJet 5550 printer (17pl drop size @ 1200dpi) [8]. The reactive inks were printed onto paper, one pass for each ink, up to a maximum of 4x2 layers. Attempts to print more layers was hindered by the raised image passing through the paper feed mechanism of the printer. The two inks were contained in different cartridges and were interchanged after each print pass.

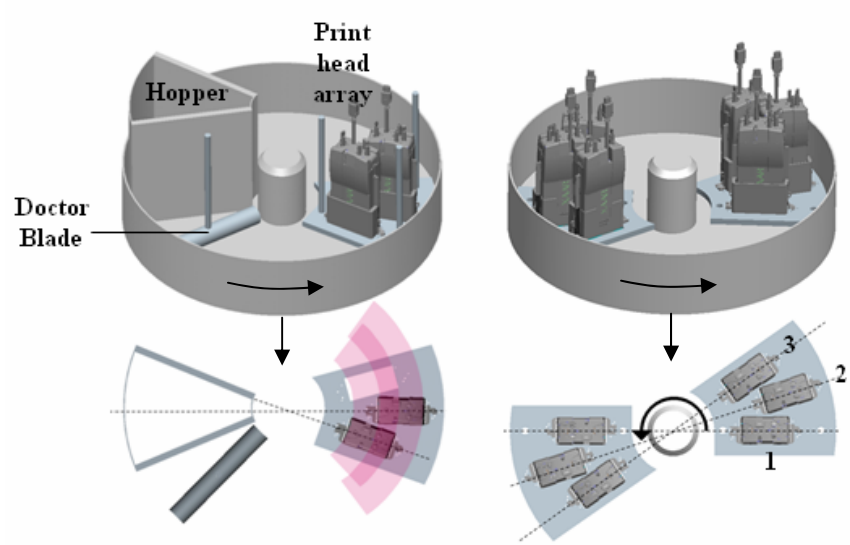

Figure 7: Schematic diagram showing SGM build drum, position of print head arrays and powder processing equipment.

Results and Discussion

Software tools have been developed to transform images in preparation for accurate reproduction onto a rotating substrate. A Typical example of a transformed image and its printed form is shown in Figure 8. In Figure 8, the print quality from print head 2 is deliberately low to highlight the circular path taken by the substrate as it passed under the print head. There are still some issues when trying to seamlessly rejoin an image when printed across two print heads. However, the authors believe this is principally a print head alignment issue rather than being associated with software errors. The size accuracy in, *x*, of transformed images printed onto paper was ±0.1mm of their predicted size. The printed image size accuracy in, *y*, is less accurately defined because it has to be scaled according to equation 2 and is a function of radial position, image size and encoder divide value, $e_n d$. Dimensional measurement analysis on a wide sample of regular quadrilaterals printed at different radial positions were typically within ±0.2mm (this value appeared to be independent of image size). The diagonal deviation (squareness) of printed images was typically ±0.5%.

The screening algorithm was used to model the radial print density variation across the total print swathe, px_{max}. For the print swathe settings described in this work, the total print density drop was calculated to be 35% (see Figure 9) and the rate of change with, *px*, followed the curve shown in Figure 6. For comparison, the grey level intensity drop measured using Photoshop™ was 27% for the same sample image. The disparity may result from the level of software interpretation when digitising printed images. Visually, screened images ordinarily looked to be corrected, although perhaps marginally over corrected at lower values of, *cx* (see Figure 9b). In an attempt to quantify the efficacy of the screen algorithm, screened printed images were digitised and examined using Photoshop™. Results suggested the print density variation was reduced to 4% across the total print swathe.

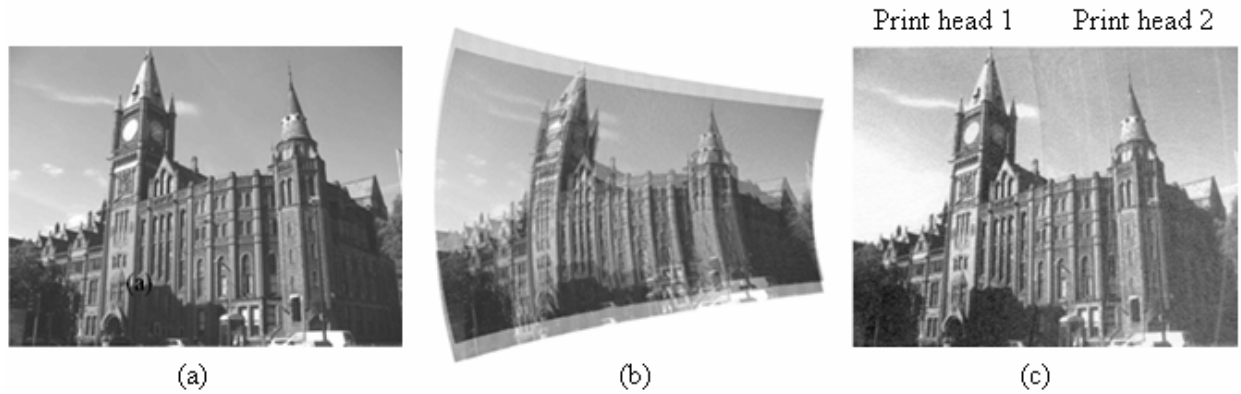

Figure 8: (a) Digitised 8 bit greyscale image, (b) transformed image and (c) image printed using SGM apparatus.

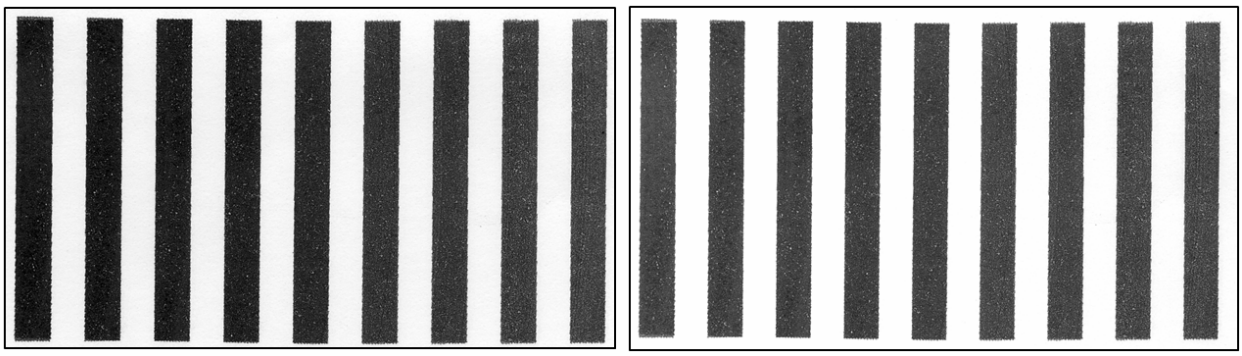

Figure 9: SGM printed image of size 1200x700 px (a) without screen and (b) with screening.

Two part reactive inks were demonstrated by overprinting the same image twice (see Figure 10); each pass using a different ink. The reaction was instantaneous giving solid precipitates of plaster which fully dried to give a relative smooth solid layer. The average layer thickness was 25µm and the density of the plaster image approached 70% (compared with compacted plaster powder); density measurements were taken using four layer samples (4x2 passes). For comparison, current 3D printing technologies tend to achieve 50-60% density from the machine. The printed plaster was also unexpectedly flexible and showed no signs of cracking when bending the paper; even to a sharp right angle. Trials are currently in development to adapt these inks for use in forthcoming versions of the Xaar print heads. It is anticipated that the SGM system will give greater flexibility over the choice of layer thickness and material density since the drop volume and print density is more adaptable than in the HP printer.

Conclusions

This paper has briefly reviewed developments in three dimensional printing and highlighted the need to develop the technology for more efficient and faster layer construction. To this end, the development of the spiral growth manufacturing process for the three dimensional printing was conceived. However, printing onto a rotating substrate poses a number of issues; namely the accurate reproduction of digital images. Therefore, the work of this paper focussed on a number of transformation and screening algorithms to prepare 8 bit greyscale and monochrome images for rotational printing using arrays of wide format, dual nozzle row, industrial print heads. Two transformation algorithms have been presented, one to polar transform the digital image and one to offset columns of pixels for printing by nozzles in two

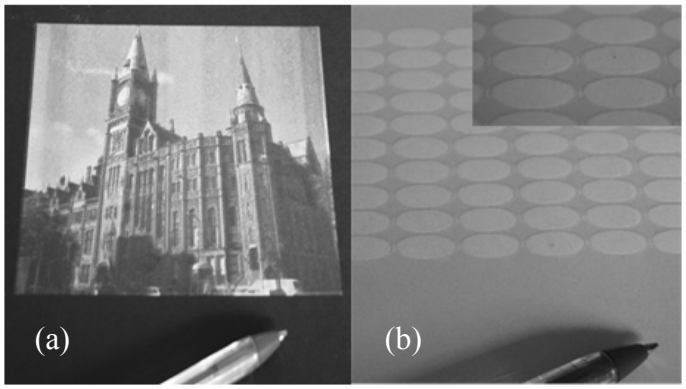

Figure 10: Reactive ink printing (a) single layer image and (b) multiple layer image (4 passes).

different parallel rows. Image reproducibility, accuracy and squareness were within reasonable limits for printing reactive inks, or binders onto powder (accuracy ±200µm, squareness ±0.5%). It is currently difficult to highlight areas where accuracy improvements can be made in the transformation algorithms. However, it is expected that more precise mechanical alignment of the print heads may lead to tolerances that equate similar to images printed on a linear conveyor. Results from the screening trials were inconclusive. Visually, the radial greyscale gradient, which is clearly visible on all images printed on the SGM apparatus appeared to be corrected after images were screened. However, the impact of radial print density variations, if any, on build quality cannot be fully evaluated until such time when reactive inks can be printed using SGM, and build geometries mechanically tested. The reactive inks show great promise, particularly for use in SGM, and would exploit the speed potential of a rotary system (minimum of 30 layers per minute build rate). Preliminary tests on the printed plaster layers suggest the material has good strength, density, wear resistance and bonds extremely well to underlying layers.

Acknowledgements

This work has been supported by grants from the UK Engineering and Physical Sciences Research Council (EPSRC). In particular, thanks must be given to Martin Dunschen and Julian Todd from FreeSteel, UK, for their help in developing the transformation algorithms. One of us (C.H.) is grateful to Martin for his training in computer programming.

References

[1] Jacobs, PF (1996). Stereolithography and other RP&M technologies. ASME Press, New York.

[2] Sachs, E., Cornie, J., Brancazio, D., Bredt, J., Curodeau, A., Fan, T., Lauder, A., Lee, J. and Michaels, S. (1993). Three dimensional printing: the physics and implications of additive manufacturing. CIRP Annals, Vol.42, 1, pp. 257-260.

[3] Sachs, E., Cima, M., Williams, P., Brancazio, D. and Cornie, J. (1992). Transactions of ASME: Journal of Engineering Industry. November, Vol. 114, pp.481-488.

[4] Cooper, K.G., Williams, G., Salvail, P. (2002). Evaluating RP Methods: NASA's Side-by-Side Comparison. Proceedings Modern Casting, Feb. 2002, pp 28-30.

[5] Noorani, R.I. (2006). Rapid Prototyping - Principles and Applications. John Wiley & Sons. pp. 123.

[6] Lutz, M. (2001). Programming Python – 2nd Edition. O'Reilly Media. ISBN 978-0596000851

[7] http://www.python.org

[8] www.HP.com